https://doi.org/10.1038/s41586-019-1144-0

XFEL structures of the human MT_2 melatonin receptor reveal the basis of subtype selectivity

Linda C. Johansson[1,2,14], Benjamin Stauch[1,2,14], John D. McCorvy[3,13], Gye Won Han[1,2], Nilkanth Patel[1,4], Xi-Ping Huang[3,5], Alexander Batyuk[6], Cornelius Gati[7,8], Samuel T. Slocum[3,5], Chufeng Li[9,10], Jessica M. Grandner[1,4], Shuming Hao[1,2], Reid H. J. Olsen[3], Alexandra R. Tribo[3], Sahba Zaare[9], Lan Zhu[10], Nadia A. Zatsepin[9,10], Uwe Weierstall[9,10], Saïd Yous[11], Raymond C. Stevens[1,2,4], Wei Liu[10], Bryan L. Roth[3,5,12]*, Vsevolod Katritch[1,2,4]* & Vadim Cherezov[1,2,4]*

The human MT_1 and MT_2 melatonin receptors[1,2] are G-protein-coupled receptors (GPCRs) that help to regulate circadian rhythm and sleep patterns[3]. Drug development efforts have targeted both receptors for the treatment of insomnia, circadian rhythm and mood disorders, and cancer[3], and MT_2 has also been implicated in type 2 diabetes[4,5]. Here we report X-ray free electron laser (XFEL) structures of the human MT_2 receptor in complex with the agonists 2-phenylmelatonin (2-PMT) and ramelteon[6] at resolutions of 2.8 Å and 3.3 Å, respectively, along with two structures of function-related mutants: $H208^{5.46}A$ (superscripts represent the Ballesteros–Weinstein residue numbering nomenclature[7]) and $N86^{2.50}D$, obtained in complex with 2-PMT. Comparison of the structures of MT_2 with a published structure[8] of MT_1 reveals that, despite conservation of the orthosteric ligand-binding site residues, there are notable conformational variations as well as differences in [^{3}H]melatonin dissociation kinetics that provide insights into the selectivity between melatonin receptor subtypes. A membrane-buried lateral ligand entry channel is observed in both MT_1 and MT_2, but in addition the MT_2 structures reveal a narrow opening towards the solvent in the extracellular part of the receptor. We provide functional and kinetic data that support a prominent role for intramembrane ligand entry in both receptors, and suggest that there might also be an extracellular entry path in MT_2. Our findings contribute to a molecular understanding of melatonin receptor subtype selectivity and ligand access modes, which are essential for the design of highly selective melatonin tool compounds and therapeutic agents.

To improve the low surface expression and stability of wild-type MT_2, we introduced eight point mutations on the basis of homology to other class A receptors: $D86^{2.50}N$ (ref. [9]), $L108^{ECL1}F$, $F129^{3.41}W$ (ref. [10]), $N137^{3.49}D$, $C140^{3.52}L$, $W264^{6.48}F$, $A305^{7.50}P$, and $N312^{8.47}D$; these were essential for determination of the high-resolution structure of both MT_2 and MT_1[8]. To promote crystal contacts, we used a double-fusion approach, with rubredoxin[11] in the intracellular loop 3 (ICL3) and thermostabilized apocytochrome b_{562}RIL (BRIL)[11] attached to the receptor N terminus. Radioligand binding assays revealed a 120-fold reduction in melatonin binding affinity (approximately 30-fold reduction at physiological concentration of NaCl), probably owing to stabilization of the crystallized construct in an inactive 'low agonist affinity' state that is deficient in G-protein coupling and signalling[9,12] (Extended Data Table 1). All four MT_2 structures were obtained using lipidic cubic phase (LCP)[13] crystallization (Extended Data Fig. 1, Extended Data Table 2). The overall receptor conformation was similar in all four structures (Cα root mean squared deviation (r.m.s.d.) < 0.3 Å), so we used the highest resolution MT_2–2-PMT structure in the analysis below unless otherwise noted.

MT_2 adopts the canonical seven-transmembrane-domain (7TM) fold of class A receptors, with the short amphipathic helix VIII parallel to the membrane on the intracellular side (Fig. 1a). As in MT_1[8], the 7TM bundle of MT_2 is found in an inactive conformation. Restoration of the function-impairing $D86^{2.50}N$ mutation (Extended Data Table 3) allowed us to solve the MT_2(N86D)–2-PMT structure at a lower resolution and showed that this mutation had no major effect on the overall

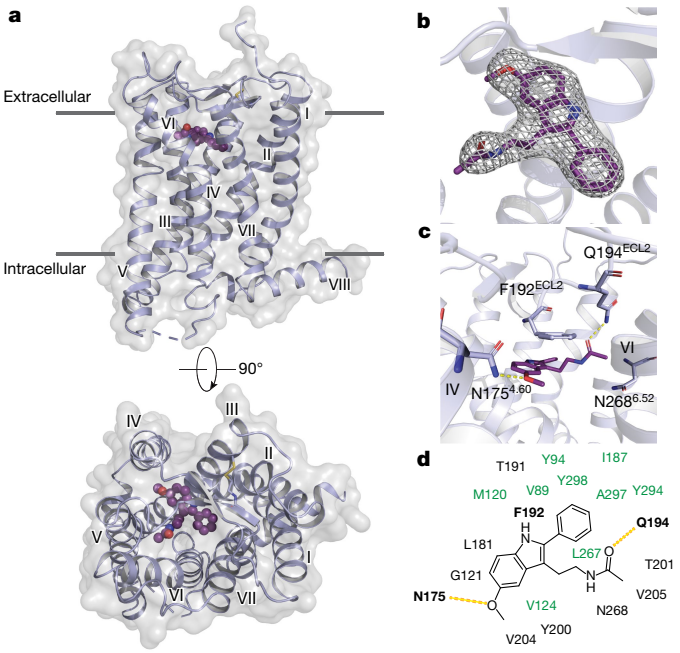

Fig. 1 | Overview of the MT_2 structure. a, Overview of MT_2 (violet) shows the canonical 7TM topology, with the ligand 2-PMT (purple) in the binding pocket. A 90° view shows the receptor from the extracellular side. Approximate membrane boundaries are shown as grey lines. **b**, $2mF_o - DF_c$ density (grey mesh) of 2-PMT contoured at 1σ. **c**, Binding pocket with key ligand interaction residues. **d**, Schematic diagram of ligand-interacting residues. Residues in the hydrophobic subpocket are coloured green. Hydrogen bonds are shown as dashed yellow lines in **c**, **d**.

[1]Bridge Institute, USC Michelson Center for Convergent Biosciences, University of Southern California, Los Angeles, CA, USA. [2]Department of Chemistry, University of Southern California, Los Angeles, CA, USA. [3]Department of Pharmacology, University of North Carolina at Chapel Hill, Chapel Hill, NC, USA. [4]Department of Biological Sciences, University of Southern California, Los Angeles, CA, USA. [5]National Institute of Mental Health Psychoactive Drug Screening Program, University of North Carolina at Chapel Hill, Chapel Hill, NC, USA. [6]Linac Coherent Light Source, SLAC National Accelerator Laboratory, Menlo Park, CA, USA. [7]Bioscience Division, SLAC National Accelerator Laboratory, Menlo Park, CA, USA. [8]Department of Structural Biology, Stanford University, Stanford, CA, USA. [9]Department of Physics, Arizona State University, Tempe, AZ, USA. [10]School of Molecular Sciences and Biodesign Center for Applied Structural Discovery, Biodesign Institute, Arizona State University, Tempe, AZ, USA. [11]Université de Lille, CHU Lille, Inserm, UMR-S 1172 - JPArc - Centre de Recherche Jean-Pierre AUBERT Neurosciences et Cancer, Lille, France. [12]Division of Chemical Biology and Medicinal Chemistry, Eshelman School of Pharmacy, University of North Carolina at Chapel Hill, Chapel Hill, NC, USA. [13]Present address: Department of Cell Biology, Neurobiology and Anatomy, Medical College of Wisconsin, Milwaukee, WI, USA. [14]These authors contributed equally: Linda C. Johansson, Benjamin Stauch. *e-mail: bryan_roth@med.unc.edu; katritch@usc.edu; cherezov@usc.edu

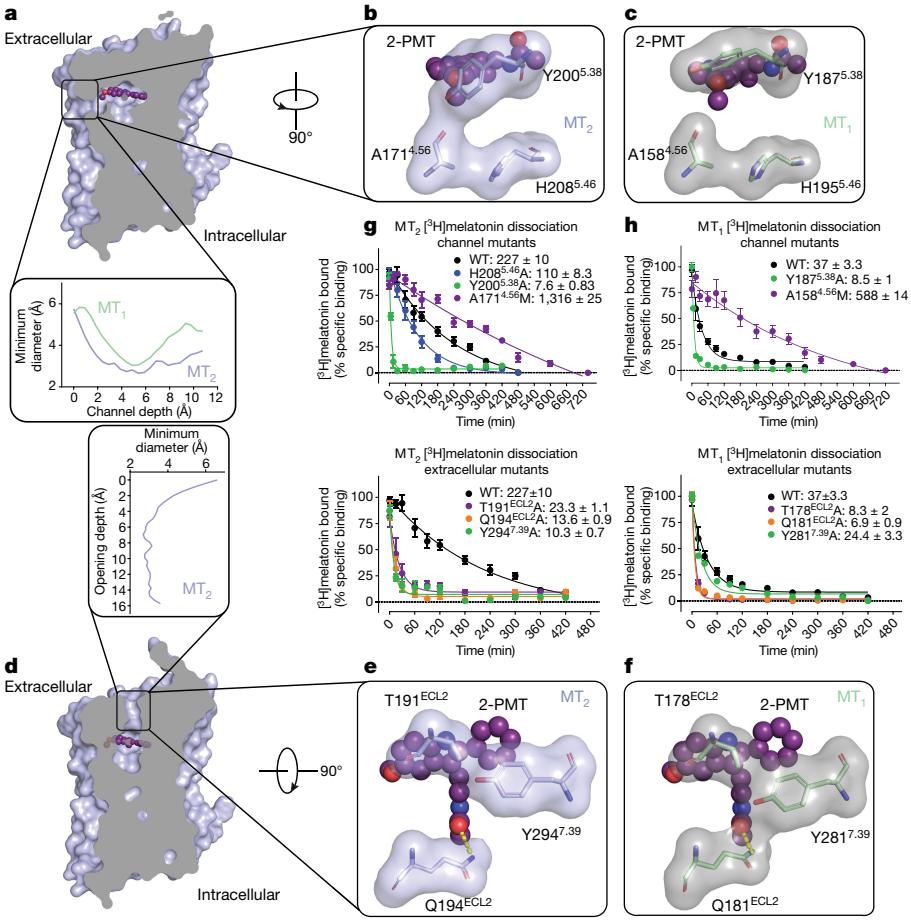

Fig. 2 | Two possible ligand entries in MT_2. a, View of the membrane-buried channel in MT_2. Inset, channel diameter profile across its length for MT_1 and MT_2. **b**, A 90° view of the channel in MT_2, highlighting three residues discussed in the text. **c**, The same view as in **b** of MT_1 (green) showing a different conformation of $Y187^{5.38}$ that widens the channel compared to MT_2. **d**, View of the ECL opening found in MT_2 (violet) with 2-PMT (purple). Inset, ECL opening profile across the length. **e**, A 90° view through the ECL opening in MT_2, highlighting three residues discussed in the text. **f**, The same view as in **e** of MT_1 (green), showing a different conformation of $Y281^{7.39}$ that seals the ECL opening. **g**, [^{3}H] Melatonin dissociation kinetics for MT_2 membrane channel mutants (top) and ECL opening mutants (bottom). **h**, As in **g** for MT_1. Residence time (k_{off}^{-1}) in **g** and **h** is given in minutes. Data are shown as mean ± s.e.m. for $n = 3$ independent experiments.

receptor conformation, as also supported by molecular dynamics sim-ulations (Supplementary Fig. 1). Structural comparison of MT_2 and MT_1—which share 68% sequence identity—revealed notable overall similarity (Cα r.m.s.d. < 0.6 Å), with all ligand-interacting residues conserved[8] (Fig. 1d, Extended Data Fig. 2c). There is a common phar-macophore between receptor subtypes that consists of aromatic stack-ing of the ligand core with $F192^{ECL2}$, as well as hydrogen bonds between the methoxy group of 2-PMT and $N175^{4.60}$ and between the alkyla-mide tail of the ligand and $Q194^{ECL2}$ (Fig. 1c, d). The stability of these ligand-anchoring interactions was confirmed by molecular dynamics simulations (Extended Data Fig. 3). Further, mutation of $F192^{ECL2}$ to isoleucine or alanine caused loss of ligand binding and signalling (Extended Data Tables 1, 4), as also observed for MT_1[8]. In contrast to MT_1, however, mutation of $N175^{4.60}$ to alanine in MT_2 did not impair receptor function, which indicates that this residue has different roles in the activation of the two receptor subtypes. Mutation of either $Q194^{ECL2}$ or $N268^{6.52}$ to alanine had only minor effects on receptor ligand affinity, receptor activation or stability (Extended Data Tables 1, 4, 5), whereas the double mutation $Q194^{ECL2}$A/$N268^{6.52}$A results in a marked loss of receptor activity (Extended Data Tables 4, 5), which suggests that these residues show functional redundancy in MT_2. Notably, despite the binding site residues being conserved between the two receptors, we observed subtle conformational differences between them, such as in the side chains of $Y200^{5.38}$ and $Y294^{7.39}$ and in the backbone region surrounding $P174^{4.59}$ (Extended Data Fig. 2d). Furthermore, the binding pocket of MT_2 is about 50 Å^3 (7%) larger than that of MT_1, with most of the volume difference attributed to the region around the alkylamide tail and the hydrophobic subpocket that accommodates substituents of melatonin analogues in our structures (Fig. 1d, Extended Data Fig. 2b). These regions have a key role in MT_2 selectivity, as discussed below.

Structural analysis of MT_2 revealed an opening between helices IV and V from the orthosteric ligand binding site to the membrane (Fig. 2a). This channel is similar to that seen in MT_1, but is more constricted (around 2.6 Å in diameter at the narrowest part). Comparison of the structures of MT_2 and MT_1 revealed that $Y200^{5.38}$ in MT_2 makes a hydrogen bond to $N175^{4.60}$, constricting the channel, whereas in MT_1 it adopts a different conformation, pointing towards the lipid interface (Fig. 2a–c, Extended Data Fig. 2c, d). In our MT_2(H208A)–2-PMT structure, mutating $H208^{5.46}$ near the channel entrance to alanine further closes off the opening by an approximately 0.9 Å inward shift of helix V (Extended Data Fig. 4). This finding suggests that $H208^{5.46}$ helps to control the channel entrance, albeit only moderately influencing ligand affinity and receptor function in MT_2 (Extended Data Tables 1, 4). Further analysis of the MT_2 structures revealed a potential secondary access route to the orthosteric binding site from the solvent-exposed extracellular (ECL) region (Fig. 2d). This second opening has a slightly larger diameter (about 2.5–3 Å) and is lined by aromatic $Y294^{7.39}$ and hydrophilic $T191^{ECL2}$ and $Q194^{ECL2}$ residues (Fig. 2e). In MT_1, the corresponding residues $Q181^{ECL2}$ and $Y281^{7.39}$ adopt different conformations, completely sealing off this entrance (Fig. 2f).

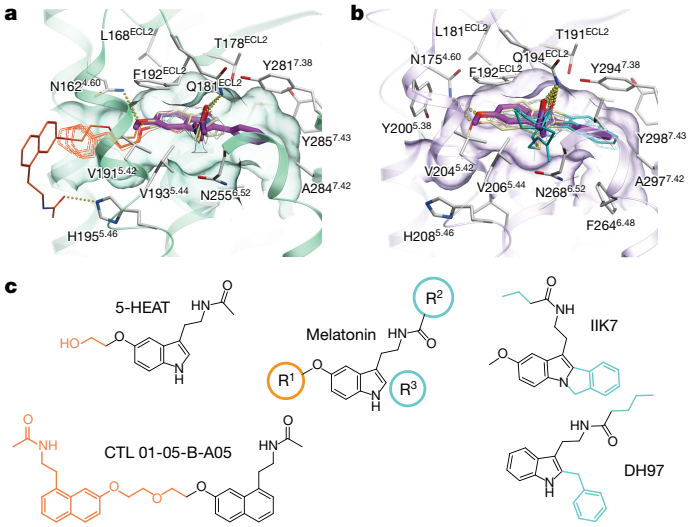

Fig. 3 | Selectivity determinants of ligands at MT_1 and MT_2. **a**, Docking of selective ligands into MT_1 (green), with 2-PMT (purple) from the crystal structure shown as reference. Ligands selective for MT_1 (compounds 63, 64, 65a, and 65b)[17] are shown in grey. Two representative ligands, 5-HEAT[16] and CTL 01-05-B-A05[8] are coloured pale yellow, with their selectivity-conferring substituents (R^1 position) shown in orange. **b**, Docking of ligands into MT_2 (violet), with 2-PMT (purple) shown as reference. Non-selective (tasimelteon, TIK301[17]) and selective (UCM1014[20], K185[17], and 4P-PDOT[17]) ligands are shown in grey. Two representative ligands, DH97[18] and IIK7[17] are coloured pale yellow, with selectivity-conferring substituents (R^2 and R^3 positions) shown in cyan. Predicted hydrogen bonds are shown as dotted lines in **a**, **b**. **c**, Melatonin SAR, in which R^1 substituents confer MT_1 selectivity (orange), and substituents in R^2 and R^3 positions confer MT_2 selectivity (cyan). See Supplementary Table 1 for a list of all docked ligands.

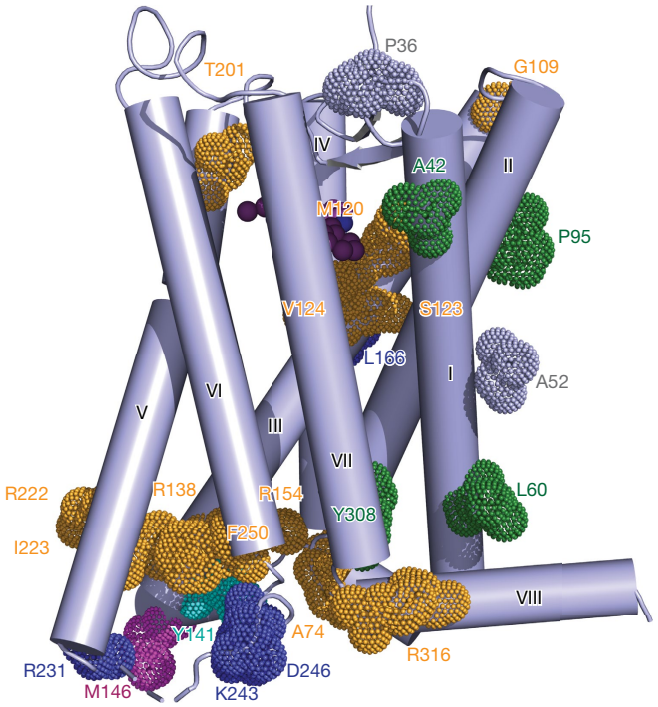

Fig. 4 | MT_2 mutations implicated in type 2 diabetes. Mapping of residues implicated in type 2 diabetes[4,5] onto the MT_2 crystal structure. Gold, residues in which mutations lead to defects in two or more pathways; cyan, G-protein-specific defects; blue, β-arrestin-2-specific defects; magenta, ERK-specific defects; green, mutations that abolish melatonin binding; grey, mutations similar to the wild type. Type-2-diabetes-related mutations in residues not observed in the crystal structure are not shown.

To test the relative importance of these two putative binding site access routes, we performed kinetic ligand dissociation studies on both receptors using [^{3}H]melatonin as a tracer. The ligand residence time (k_{off}^{-1}) is substantially longer in wild-type MT_2 than in MT_1, which suggests that the narrower membrane entry channel restricts ligand access (Fig. 2g, h). Mutation of the membrane channel-lining residue $Y^{5.38}A$, designed to widen the access channel, caused a 30-fold decrease in residence time for MT_2 (with similar ligand affinity), while the corresponding mutation in MT_1 caused a more-modest decrease in residence time, consistent with the wider channel and a different conformation of $Y^{5.38}$ in MT_1. To constrict the channel, we mutated $A^{4.56}$, a key residue at the interface of helices IV and V in both receptors, into a bulkier methionine. This mutation markedly increased residence time for both receptors (Fig. 2g, h), reaching up to 20 h in MT_2, which suggests that this channel is important for ligand access in both receptors.

When we tested mutations designed to widen the ECL opening in both receptors, ligand residence time was reduced more than tenfold in MT_2 mutants $T191^{ECL2}A$ and $Q194^{ECL2}A$, and roughly fivefold with the equivalent ECL2 mutations in MT_1 (Fig. 2g, h). The $MT_2(Y294^{7.39}A)$ mutant showed an even greater decrease in ligand residence time (22-fold) relative to the wild type, whereas the equivalent MT_1 mutant showed a similar residence time to the wild type. These differences can be reconciled if ligand site access through the ECL entrance is more important in MT_2 than in MT_1, consistent with the crystal structures, in which residue $Y294^{7.39}$ adopts a different conformation in MT_2, allowing easier ligand egress through the ECL opening.

The elucidation of high-resolution structures of both melatonin receptor subtypes and published ligand structure–activity relationship (SAR) data[14,15] allowed us to establish a model of receptor subtype ligand selectivity. To this end, we used molecular docking of several available selective ligands to both receptors. Docking of the moderately MT_1-selective compound 5-hydroxyethoxy-*N*-acetyltryptamine (5-HEAT)[16] and the bitopic ligand CTL 01-05-B-A05[8] suggests that—although an extension or substitution of the R^1 position by a linear alkyl chain can be accommodated by the membrane access channel in both MT_1 and MT_2 (Fig. 3a, c)—the narrower MT_2 channel renders binding of the extended portion of the bitopic ligands suboptimal owing to potential steric clashes. Accordingly, the $H208^{5.46}A$ mutation in MT_2 abolished the efficacy of CTL 01-05-B-A05 as a G_i agonist (Extended Data Fig. 4d), probably by further restricting the channel and/or eliminating the hydrogen bond between $H208^{5.46}$ and CTL 01-05-B-A05 that was observed in docking to MT_1[8]. This mutation had a negligible effect on monotopic ligand binding and function (Extended Data Tables 1, 4, 5), which suggests that a sufficiently wide membrane channel (as in MT_1) is essential for accommodation of bitopic ligands.

The MT_2-selective ligands IIK7 and DH97 (both of which are about 90-fold selective)[17,18] adopt 'tail up' binding modes similar to that of 2-PMT, with their alkylamide tails (R^2 position in Fig. 3b, c) interacting with $Q194^{ECL2}$. By contrast, in MT_1 the longer alkylamide tails of these ligands avoid this upward tail position owing to steric clashes, and can adopt only suboptimal 'tail down' conformations. Bulky substituents in the R^3 position confer MT_2 selectivity by using the larger hydrophobic subpocket of the receptor (Fig. 3b, c). In summary, our analysis suggests that R^1 substituents are important for MT_1 selectivity, while R^2 and R^3 mostly convey selectivity towards MT_2 (Fig. 3c). The slightly larger binding site in MT_2 also helps to achieve selectivity, as reflected by the larger number of compounds that are moderately selective for MT_2 (Extended Data Fig. 5).

Subtype-selective compounds are desirable owing to the involvement of MT_2 in type 2 diabetes, for which a number of single nucleotide polymorphisms (SNPs) have been reported[4,5]. When we mapped these sites onto our MT_2 structure, we observed clustering of residues in the vicinity of the ligand binding pocket and on the receptor surface, along the membrane interface of helices I and II and the intracellular G-protein and β-arrestin binding regions (Fig. 4). The exposed positions

of these residues could point to their involvement in interactions with intracellular and membrane partners. Other instances of SNPs associated with type 2 diabetes include P95$^{2.59}$L of the YPYP motif, which is involved in receptor stability and function in MT_1[8], and mutations in known microswitches such as R138$^{3.50}$H/L/C of the E/DRY motif[19] and Y308$^{7.53}$S of the NPXXY motif[12]. Although none of the analysed SNPs is involved in direct interactions with melatonin, the M120$^{3.32}$I/V and V124$^{3.36}$I variants are located in the hydrophobic subpocket of the receptor, which could influence ligand binding and affect subsequent signalling pathways[4,5].

The structural basis of melatonin receptor subtype selectivity revealed here has the potential to inspire a new generation of highly selective pharmacological tools that will help to further dissect the melatonin system. We also provide insights into differences in ligand entry between the two receptors by demonstrating the potential of MT_2 to support extracellular ligand access to the binding pocket. This difference in ligand entry can be exploited to facilitate melatonin receptor subtype selectivity, as the ECL route in MT_2 could accommodate more polar compounds compared to the membrane-buried channel. We therefore expect that our results will lead to new therapies involving these pleiotropic receptors, aimed at—but not limited to—the treatment of type 2 diabetes, cancer and sleep disorders.

Online content

Any methods, additional references, Nature Research reporting summaries, source data, statements of data availability and associated accession codes are available at https://doi.org/10.1038/s41586-019-1144-0.

Received: 28 July 2018; Accepted: 26 March 2019;
Published online 24 April 2019.

1. Reppert, S. M., Weaver, D.R. & Ebisawa, T. Cloning and characterization of a mammalian melatonin receptor that mediates reproductive and circadian responses. *Neuron* **13**, 1177–1185 (1994).
2. Reppert, S. M. et al. Molecular characterization of a second melatonin receptor expressed in human retina and brain: the Mel1b melatonin receptor. *Proc. Natl Acad. Sci. USA* **92**, 8734–8738 (1995).
3. Liu, J. et al. MT1 and MT2 melatonin receptors: a therapeutic perspective. *Annu. Rev. Pharmacol. Toxicol.* **56**, 361–383 (2016).
4. Bonnefond, A. et al. Rare MTNR1B variants impairing melatonin receptor 1B function contribute to type 2 diabetes. *Nat. Genet.* **44**, 297–301 (2012).
5. Karamitri, A. et al. Type 2 diabetes-associated variants of the MT2 melatonin receptor affect distinct modes of signaling. *Sci. Signal.* **11**, eaan6622 (2018).
6. Kato, K. et al. Neurochemical properties of ramelteon (TAK-375), a selective MT1/MT2 receptor agonist. *Neuropharmacology* **48**, 301–310 (2005).
7. Ballesteros, J. A. & Weinstein, H. Integrated methods for the construction of three-dimensional models and computational probing of structure-function relations in G protein-coupled receptors. *Meth. Neurosci.* **25**, 366–428 (1995).
8. Stauch, B. et al. Structural basis of ligand recognition at the human MT1 melatonin receptor. *Nature* https://doi.org/10.1038/s41586-019-1141-3 (2019).
9. White, K. L. et al. Structural connection between activation microswitch and allosteric sodium site in GPCR signaling. *Structure* **26**, 259–269.e5 (2018).
10. Roth, C. B., Hanson, M. A. & Stevens, R. C. Stabilization of the human β2-adrenergic receptor TM4–TM3–TM5 helix interface by mutagenesis of Glu122$^{3.41}$, a critical residue in GPCR structure. *J. Mol. Biol.* **376**, 1305–1319 (2008).
11. Chun, E. et al. Fusion partner toolchest for the stabilization and crystallization of G protein-coupled receptors. *Structure* **20**, 967–976 (2012).
12. Audet, M. & Bouvier, M. Restructuring G-protein- coupled receptor activation. *Cell* **151**, 14–23 (2012).
13. Caffrey, M. & Cherezov, V. Crystallizing membrane proteins using lipidic mesophases. *Nat. Protocols* **4**, 706–731 (2009).
14. Rivara, S., Mor, M., Bedini, A., Spadoni, G. & Tarzia, G. Melatonin receptor agonists: SAR and applications to the treatment of sleep-wake disorders. *Curr. Top. Med. Chem.* **8**, 954–968 (2008).
15. Bento, A. P. et al. The ChEMBL bioactivity database: an update. *Nucleic Acids Res.* **42**, D1083–D1090 (2014).
16. Nonno, R. et al. A new melatonin receptor ligand with mt1-agonist and MT2-antagonist properties. *J. Pineal Res.* **29**, 234–240 (2000).
17. Zlotos, D. P., Jockers, R., Cecon, E., Rivara, S. & Witt-Enderby, P. A. MT1 and MT2 melatonin receptors: ligands, models, oligomers, and therapeutic potential. *J. Med. Chem.* **57**, 3161–3185 (2014).
18. Teh, M. T. & Sugden, D. Comparison of the structure-activity relationships of melatonin receptor agonists and antagonists: lengthening the N-acyl side-chain has differing effects on potency on *Xenopus* melanophores. *Naunyn Schmiedebergs Arch. Pharmacol.* **358**, 522–528 (1998).
19. Valentin-Hansen, L. et al. The arginine of the DRY motif in transmembrane segment III functions as a balancing micro-switch in the activation of the β2-adrenergic receptor. *J. Biol. Chem.* **287**, 31973–31982 (2012).
20. Spadoni, G. et al. Highly potent and selective MT2 melatonin receptor full agonists from conformational analysis of 1-benzyl-2-acylaminomethyl-tetrahydroquinolines. *J. Med. Chem.* **58**, 7512–7525 (2015).

Acknowledgements We thank M. Chu, C. Hanson, K. Villers, and J. Velasquez for help with cloning and expression, T. Grant for XFEL data processing, and H. Shaye for technical support. This work was supported by the National Institutes of Health grants R35 GM127086 (V.C.), R21 DA042298 (W.L.), R01 GM124152 (W.L.), U24DK116195 (B.L.R.), R01MH112205 (B.L.R.), the NIMH Psychoactive Drug Screening Program and the Michael Hooker Distinguished Professorship to B.L.R. and F31-NS093917 (R.H.J.O.), the STC Program of the National Science Foundation (NSF) through BioXFEL (No. 1231306) (B.S., U.W., W.L., N.A.Z., V.C.), NSF ABI grant 1565180 (C.L, N.Z., U.W.), HFSP long-term fellowship LT000046/2014-L (L.C.J.), postdoctoral fellowship from the Swedish Research Council (L.C.J.) and EMBO ALTF 677-2014 (B.S.). Parts of this research were carried out at the LCLS, a National User Facility operated by Stanford University on behalf of the US Department of Energy and supported by the US Department of Energy Office of Science, Office of Basic Energy Sciences under Contract No. DE-AC02-76SF00515. This research benefited from the use of credits from the National Institutes of Health (NIH) Cloud Credits Model Pilot, a component of the NIH Big Data to Knowledge (BD2K) program.

Reviewer information *Nature* thanks Christian Siebold, Ieva Sutkeviciute, Jean-Pierre Vilardaga and the other anonymous reviewer(s) for their contribution to the peer review of this work.

Author contributions L.C.J., B.S., V.K., and V.C. conceived the project, analysed data, and wrote the paper with contributions from all authors. L.C.J. and B.S. designed, optimized, purified and characterized receptor constructs for structural studies and crystallized the receptor, prepared crystal samples and figures, solved and refined the structures, and assisted in generating mutant constructs for binding and functional analyses. J.D.M., X.-P.H., and S.T.S. performed radioligand binding and functional experiments, assisted in making mutant and wild-type constructs, and analysed binding and functional data. L.C.J., B.S., A.B., L.Z., W.L., and V.C. collected XFEL data. S.Z. and U.W. operated the LCP injector during XFEL data collection. S.H., L.Z., and W.L. assisted in XFEL sample preparation. A.B., C.G., C.L., and N.A.Z. processed XFEL data. L.C.J., G.W.H. and A.B. determined the structures. L.C.J. and G.W.H. performed the structure refinement and quality control. N.P., J.M.G., and V.K. designed mutants for radioligand and functional studies, and performed molecular docking and molecular dynamics simulations. R.H.J.O. and A.R.T. assisted with molecular biology and functional experiments. S.Y. synthesized the bitopic compound, analysed data, and edited the paper. R.C.S. contributed to study design and selection of chemical compounds for receptor stabilization and functional characterization, supervised protein expression, and edited the paper. B.L.R. supervised pharmacological experiments and edited the paper. V.K. supervised molecular docking and molecular dynamics calculations. V.C. coordinated and supervised the whole project.

Competing interests The authors declare no competing interests.

Additional information
Extended data is available for this paper at https://doi.org/10.1038/s41586-019-1144-0.
Supplementary information is available for this paper at https://doi.org/10.1038/s41586-019-1144-0.
Reprints and permissions information is available at http://www.nature.com/reprints.
Correspondence and requests for materials should be addressed to B.L.R., V.K. or V.C.
Publisher's note: Springer Nature remains neutral with regard to jurisdictional claims in published maps and institutional affiliations.

METHODS

No statistical methods were used to predetermine sample size. The experiments were not randomized and the investigators were not blinded to allocation during experiments and outcome assessment.

Design and expression of MT_2 crystallized construct. The DNA sequence of human MT_2 receptor (UniProt[21] identifier P49286) was synthesized by GenScript with optimization for expression in insect cells. The crystallized construct (MT_2-CC) has truncations of N-terminal residues 1–30 and C-terminal residues 341–362. The thermostabilized apocytochrome BRIL (UniProt P0ABE7) from *Escherichia coli* with mutations M7W, H102I and R106L was fused to the truncated N terminus of MT_2 with a six-residue linker (GDGARP). Another fusion protein, rubredoxin (Rub, UniProt P00268), was fused in ICL3, replacing receptor residues 232–240. For construct optimization (to increase monodispersity, thermostability and crystallizability), the following point mutations were added: $D86^{2.50}N^{9}$, $L108^{ECL1}F$, $F129^{3.41}W^{10}$, $N137^{3.49}D$, $C140^{3.52}L$, $W264^{6.48}F$, $A305^{7.50}P$ and $N312^{8.47}D$ (see the accompanying paper[8] for details). The MT_2-CC coding sequence was subcloned into a modified pFastBac1 (Invitrogen) vector, with a haemagglutinin (HA) signal sequence and a Flag tag on the N terminus and a PreScission protease cleavage site followed by a 10× His tag on the C terminus. The receptor was expressed in *Spodoptera frugiperda* cells (Sf9, purchased from ATCC, CRL-1711, authenticated by supplier using morphology and growth characteristics, certified mycoplasma-free), which were collected and stored as described in the accompanying paper[8].

Purification of MT_2-CC. Insect cell membranes were prepared by thawing frozen cell pellets in a hypotonic buffer containing 10 mM HEPES (pH 7.5), 10 mM $MgCl_2$, 20 mM KCl, and homemade protease inhibitor cocktail. Extensive washing of the raw membranes was performed by repeated Dounce homogenization and centrifugation in hypotonic buffer (once), followed by high osmotic buffer containing 1.0 M NaCl, 10 mM HEPES (pH 7.5), 10 mM $MgCl_2$, 20 mM KCl, and homemade protease inhibitor cocktail (two or three times), thereby separating soluble and membrane-associated proteins from integral membrane proteins. Stocks (100 mM) of 2-PMT (Tocris) and ramelteon (Apex Biosciences) were dissolved in DMSO. Washed membranes were resuspended into a buffer containing 50 μM 2-PMT or ramelteon, 2 mg ml^{-1} iodoacetamide, and homemade protease inhibitor cocktail, and incubated at 4 °C for 30 min before solubilization. The membranes were then solubilized in 50 mM HEPES (pH 7.5), 150 mM NaCl, 1% (wt/vol) *n*-dodecyl-β-D-maltopyranoside (DDM, Anatrace), 0.2% (wt/vol) cholesteryl hemisuccinate (CHS, Sigma-Aldrich) at 4 °C for 3 h. The supernatant was isolated by centrifugation at 60,000*g* for 50 min, and incubated in 20 mM HEPES (pH 7.5), 800 mM NaCl with Talon (immobilized metal affinity chromatography IMAC) resin (Clontech) overnight at 4 °C. After binding, the resin was washed with twenty column volumes of wash buffer 1 (50 mM HEPES (pH 7.5), 50 μM 2-PMT or ramelteon, 800 mM NaCl, 10% (vol/vol) glycerol, 0.1% (wt/vol) DDM, 0.02% (wt/vol) CHS, 10 mM imidazole), followed by ten column volumes of wash buffer 2 (50 mM HEPES (pH 7.5), 50 μM 2-PMT or ramelteon, 150 mM NaCl, 10% (vol/vol) glycerol, 0.05% (wt/vol) DDM, 0.01% (wt/vol) CHS, 50 mM imidazole). The protein was then eluted in minimal volumes of elution buffer (50 mM HEPES (pH 7.5), 50 μM 2-PMT or ramelteon, 150 mM NaCl, 10% (vol/vol) glycerol, 0.02% (wt/vol) DDM, 0.01% (wt/vol) CHS, 220 mM imidazole). PD MiniTrap G-25 columns (GE Healthcare) were used to remove imidazole. The protein was then treated overnight with His-tagged PreScission protease (GenScript) to cleave the C-terminal His-tag. PreScission protease and the cleaved C-terminal fragment were removed by binding to Talon IMAC resin for 1.5 h at 4 °C. The protein was collected as the TALON IMAC column flow-through. The ligand concentration was increased to 100 μM, and the protein was concentrated to 30–40 mg ml^{-1} with a 100-kDa molecular mass cut-off Vivaspin centrifuge concentrator (Sartorius).

Protein stability assays. The stability of purified MT_2-CC was analysed using a microscale thermostability assay[22] using Rotorgene (QIAGEN). In brief, 1–5 μg of protein was mixed with 1.5 μM 7-diethylamino-3-(4′-maleimidylphenyl)-4-methylcoumarin (CPM) dye (2.5 mM stock in DMSO) in 25 mM HEPES pH 7.5, 150 mM NaCl, 0.02% DDM (wt/vol), 0.004% CHS (wt/vol), 10% glycerol (vol/vol), and indicated concentrations of compounds to a final volume of 100 μl. Samples were incubated for 15 min at 20 °C and then heated gradually from 25 °C to 95 °C at a rate of 2 °C min^{-1}, monitoring CPM fluorescence (excitation 365 nm, emission 460 nm). The melting temperature (T_m) was determined using the derivative of the resulting melting temperature curve after background subtraction using Prism 7.0 (GraphPad).

Crystallization. Purified MT_2-CC in complex with 2-PMT or ramelteon was reconstituted into LCP by mixing it with molten lipid using a mechanical syringe mixer[13]. The protein–LCP mixture contained 40% (wt/wt) receptor solution, 54% (wt/wt) monoolein, and 6% (wt/wt) cholesterol. Crystallization trials were performed in 96-well glass sandwich plates (Marienfeld) using an NT8-LCP robot (Formulatrix) by dispensing 40 nl of protein-laden LCP and 800 nl of precipitant solution per well. Plates were incubated and imaged at 20 °C using an automatic incubator/imager (RockImager 1000, Formulatrix). Initial crystal hits were identified in a condition containing 100 mM HEPES, pH 6.8, 30% (vol/vol) PEG 400, 100 mM $NH_4CH_3CO_2$. These crystals, approximately 30 × 30 × 70 μm^3, were collected using micromounts (MiTeGen) and flash-frozen in liquid nitrogen for data collection at a microfocus synchrotron source. After extensive optimization, the best crystals diffracted to about 3.0 Å resolution, but suffered from radiation damage, resulting in a 3.5 Å complete dataset. Additives had no effect on diffraction quality. Microcrystals for SFX data collection were prepared in gas-tight syringes (Hamilton) as previously described[23]. After optimization, diffraction-quality crystals were obtained from 100 mM ADA pH 5.8–6.5, 24–28% (vol/vol) PEG 400, 10–200 mM $NH_4CH_3CO_2$, 50 μM 2-PMT or ramelteon, by injecting 5 μl of protein-laden LCP into 50 μl precipitant in syringes. Before loading the microcrystals into the LCP injector, excess precipitant was removed and 7.9 monoacylglycerol (MAG) lipid was added to the LCP to absorb any residual precipitant solution and to prevent crystalline phase formation upon rapid cooling when injecting LCP into vacuum[24].

Crystallographic data collection. Data collection was performed at the Coherent X-ray Imaging (CXI)[25] end station of the Linac Coherent Light Source (LCLS), which operated at a wavelength of 1.3 Å (9.83 keV) delivering individual X-ray pulses of 30 and 43 fs pulse duration and approximately 10^{11} photons per pulse focused into a spot size of approximately 1.5 μm in diameter using a pair of Kirkpatrick–Baez mirrors. Microcrystals (Extended Data Fig. 1c) of MT_2 (approximately 5 × 5 × 5 μm^3) were delivered in the LCP medium using an LCP microextrusion injector[24] with 50-μm nozzle running at a flow rate of approximately 300 nl min^{-1}. Diffraction images were recorded at a rate of 7,200 patterns per minute (120 Hz) with the 2.3 Megapixel Cornell-SLAC Pixel Array Detector (CSPAD)[26]. Initial diffraction frames were corrected and filtered using the software package Cheetah[27]. A crystal 'hit' was defined as an image containing a minimum of 20 diffraction peaks with a signal-to-noise ratio above 4 and a number of pixels above 3. After further refinement of parameters (peak detection, prediction and integration), images were indexed using MOSFLM[28], DirAx[29], and XDS[30] and integrated and merged into a final dataset using CrystFEL v.0.6.2 software suite[31]. Integration radii of 3, 5, and 6 pixels with per pattern resolution cut-offs 1.0 nm^{-1} above the conservative resolution estimates for each crystal were applied (push-res option), otherwise default values were used. The total numbers of collected images/hits/indexed images are as follows: 2,154,963/84,928/31,677 (MT_2-CC–2-PMT), 476,863/59,071/28,130 (MT_2-CC(H208A)–2-PMT), 293,060/22,267/20,704 (MT_2-CC(N86D)–2-PMT), 727,004/60,005/28,834 (MT_2-CC–ramelteon). As a resolution cutoff, the criterion[32] of $CC^* > 0.5$ was used for all datasets (see Extended Data Table 2 for data statistics). The space group was determined to be $P2_1$, with two molecules per asymmetric unit.

Structure determination. To solve the 2.8 Å resolution MT_2-CC–2-PMT structure, a search model was generated as follows: the MT_2 receptor sequence was sent to the HHpred server[33], and the output models were reduced by removing all low-resolution (<3.0 Å) and NMR structures. The RCSB Protein Data Bank (PDB) files of the top ten hits were downloaded and prepared with Sculptor[34]. The models were structurally superimposed, and the side chains were pruned, yielding the conserved receptor core model. The model that produced a successful molecular replacement solution with Phaser[35] (TFZ score of 14.9 and LLG of 320) was based on the C-C chemokine receptor 2 structure (PDB ID: 5T1A)[36]. This solution containing two receptor molecules was fixed as a partial solution, and the search continued with rubredoxin (PDB ID: 1IRO), in which one molecule was placed in the asymmetric unit. The resulting three-component solution was subjected to several rounds of refining with phenix.refine[37] and model building with phenix.autobuild[38] followed by manual refinement in Coot[39]. BRIL (PDB ID: 1M6T) was then used independently as a search model for remaining fusion partners in the asymmetric unit. The second BRIL was manually modelled into the electron density; however, no density could be found for the second rubredoxin molecule, which, therefore, was not modelled in the final structure. This rubredoxin fusion partner is likely to be disordered and does not participate in crystal contacts, however, there is space for it in the crystal lattice (Extended Data Fig. 1d). A zinc ion was modelled in rubredoxin as previously described[40]. Refinement and model completion were performed by repetitive cycling between Refmac5[41] or autoBUSTER v.2.10.2[42] and manual rebuilding in Coot[39] using both $2mF_o - DF_c$ and $mF_o - DF_c$ maps. Ligand restraints for refinement of 2-PMT and ramelteon coordinates were generated by Prodrg[43]. For the other three datasets, the MT_2-CC–2-PMT structure was used as a search model for molecular replacement, and the refinement procedure was repeated as described above. The Ramachandran plot obtained by MolProbity[44] shows that, with the exception of Y92 from the YPYP motif, all residues are in the favoured/allowed regions: 95.4/4.4% of residues (MT_2-CC–2-PMT), 93/6.8% of residues (MT_2-CC(H208A)-2-PMT), 94.8/5.0% of residues (MT_2-CC(N86D)-2-PMT), 95.3/4.5% of residues (MT_2-CC–ramelteon). Data collection and refinement statistics are summarized for each structure in

Extended Data Table 2. Figures containing electron density and molecular structures were generated using PyMol[45].

Channel profile calculations. The channel diameter profile along its length was calculated with CAVER analyst v.2.0[46] using default parameters. Further details can be found in the accompanying paper[8].

Molecular docking. MT_2 receptor ligands obtained from the ChEMBL database[15] were docked into the 2-PMT-bound crystal structures using an energy based docking in ICM-Pro v3.8-6[47] as described in the accompanying paper[8].

Molecular dynamics simulations. The experimental structure of MT_2 was prepared and subjected to molecular dynamics simulations as described in the accompanying paper[8]. The simulation periodic box had dimensions (x, y, z) of 75.5 Å, 75.5 Å, 105.4 Å, and contained lipids (129 POPC molecules), 10,281 water molecules, 26 sodium ions, and 36 chloride ions.

Radioligand binding assays. Equilibrium binding assays were performed and analysed as described in the accompanying paper[8]. HEK293T cells were obtained from ATCC (CRL-11268, authenticated by supplier using morphology, growth characteristics and short tandem repeat profiling, certified mycoplasma-free). For kinetic studies, to initiate dissociation of [^{3}H]melatonin, 10 μl of cold excess melatonin (10 μM) was added per well at specific time points ranging from 2 min to 10 h, and immediately at time = 0 min plates were collected. Dissociation experiments were performed at 25 °C for MT_1 and 37 °C for MT_2 because of the slow kinetics in MT_2. For all assays, non-specific activity was defined by the addition of 5 μM 2-PMT. Ligand dissociation data were analysed using 'Dissociation-One phase exponential decay' to yield estimates of k_{off} using GraphPad Prism 7.0.

MT_2 $G_{i/o}$-mediated cAMP inhibition assay. MT_2 $G_{i/o}$-mediated cAMP inhibition assays were performed in HEK293T cells as described in the accompanying paper[8].

Reporting summary. Further information on research design is available in the Nature Research Reporting Summary linked to this paper.

Data availability

Structure factors and coordinates were deposited in the Protein Data Bank under the following accession codes: 6ME6 (MT_2-CC–2-PMT), 6ME7 (MT_2-CC(H208A)–2-PMT), 6ME8 (MT_2-CC(N86D)–2-PMT), 6ME9 (MT_2-CC–ramelteon).

21. UniProt Consortium, T. UniProt: the universal protein knowledgebase. *Nucleic Acids Res.* **46**, 2699 (2018).
22. Alexandrov, A. I., Mileni, M., Chien, E. Y., Hanson, M. A. & Stevens, R. C. Microscale fluorescent thermal stability assay for membrane proteins. *Structure* **16**, 351–359 (2008).
23. Liu, W. et al. Serial femtosecond crystallography of G protein-coupled receptors. *Science* **342**, 1521–1524 (2013).
24. Weierstall, U. et al. Lipidic cubic phase injector facilitates membrane protein serial femtosecond crystallography. *Nat. Commun.* **5**, 3309 (2014).
25. Boutet, S. W. G. J. The Coherent X-ray Imaging (CXI) instrument at the Linac Coherent Light Source (LCLS). *New J. Phys.* **12**, 035024 (2010).
26. Hart, P. et al. The CSPAD Megapixel X-ray Camera at LCLS. In *X-ray Free-electron Lasers: Beam Diagnostics, Beamline Instrumentation and Applications* (eds. S. P. Moeller, S. P. et al.) 85040C–85012 (2012).
27. Barty, A. et al. Cheetah: software for high-throughput reduction and analysis of serial femtosecond X-ray diffraction data. *J. Appl. Crystallogr.* **47**, 1118–1131 (2014).
28. Battye, T. G., Kontogiannis, L., Johnson, O., Powell, H. R. & Leslie, A. G. iMOSFLM: a new graphical interface for diffraction-image processing with MOSFLM. *Acta Crystallogr. D* **67**, 271–281 (2011).
29. Duisenberg, A. J. M. Indexing in single-crystal diffractometry with an obstinate list of reflections. *J. Appl. Crystallogr.* **25**, 92–96 (1992).
30. Kabsch, W. Xds. *Acta Crystallogr. D* **66**, 125–132 (2010).
31. White, T. A. et al. Recent developments in *CrystFEL*. *J. Appl. Crystallogr.* **49**, 680–689 (2016).
32. Karplus, P. A. & Diederichs, K. Linking crystallographic model and data quality. *Science* **336**, 1030–1033 (2012).
33. Zimmermann, L. et al. A completely reimplemented MPI bioinformatics toolkit with a new HHpred server at its core. *J. Mol. Biol.* **430**, 2237–2243 (2018).
34. Bunkóczi, G. & Read, R. J. Improvement of molecular-replacement models with Sculptor. *Acta Crystallogr. D* **67**, 303–312 (2011).
35. McCoy, A. J. et al. Phaser crystallographic software. *J. Appl. Crystallogr.* **40**, 658–674 (2007).
36. Zheng, Y. et al. Structure of CC chemokine receptor 2 with orthosteric and allosteric antagonists. *Nature* **540**, 458–461 (2016).
37. Afonine, P. V. et al. Towards automated crystallographic structure refinement with phenix.refine. *Acta Crystallogr. D* **68**, 352–367 (2012).
38. Adams, P. D. et al. PHENIX: a comprehensive Python-based system for macromolecular structure solution. *Acta Crystallogr. D* **66**, 213–221 (2010).
39. Emsley, P., Lohkamp, B., Scott, W. G. & Cowtan, K. Features and development of Coot. *Acta Crystallogr. D* **66**, 486–501 (2010).
40. Tan, Q. et al. Structure of the CCR5 chemokine receptor–HIV entry inhibitor maraviroc complex. *Science* **341**, 1387–1390 (2013).
41. Murshudov, G. N., Vagin, A. A. & Dodson, E. J. Refinement of macromolecular structures by the maximum-likelihood method. *Acta Crystallogr. D* **53**, 240–255 (1997).
42. BUSTER v. 2.10.2.
43. Schüttelkopf, A. W. & van Aalten, D. M. PRODRG: a tool for high-throughput crystallography of protein–ligand complexes. *Acta Crystallogr. D* **60**, 1355–1363 (2004).
44. Chen, V. B. et al. MolProbity: all-atom structure validation for macromolecular crystallography. *Acta Crystallogr. D* **66**, 12–21 (2010).
45. The PyMOL Molecular Graphics System. Version 2.0 Schrödinger, LLC.
46. Jurcik, A. et al. CAVER Analyst 2.0: analysis and visualization of channels and tunnels in protein structures and molecular dynamics trajectories. *Bioinformatics* **34**, 3586–3588 (2018).
47. Abagyan, R. A., Totrov, M. M. & Kuznetsov, D. A. ICM: a new method for protein modeling and design: applications to docking and structure prediction from the distorted native conformation. *J. Comput. Chem.* **15**, 488–506 (1994).

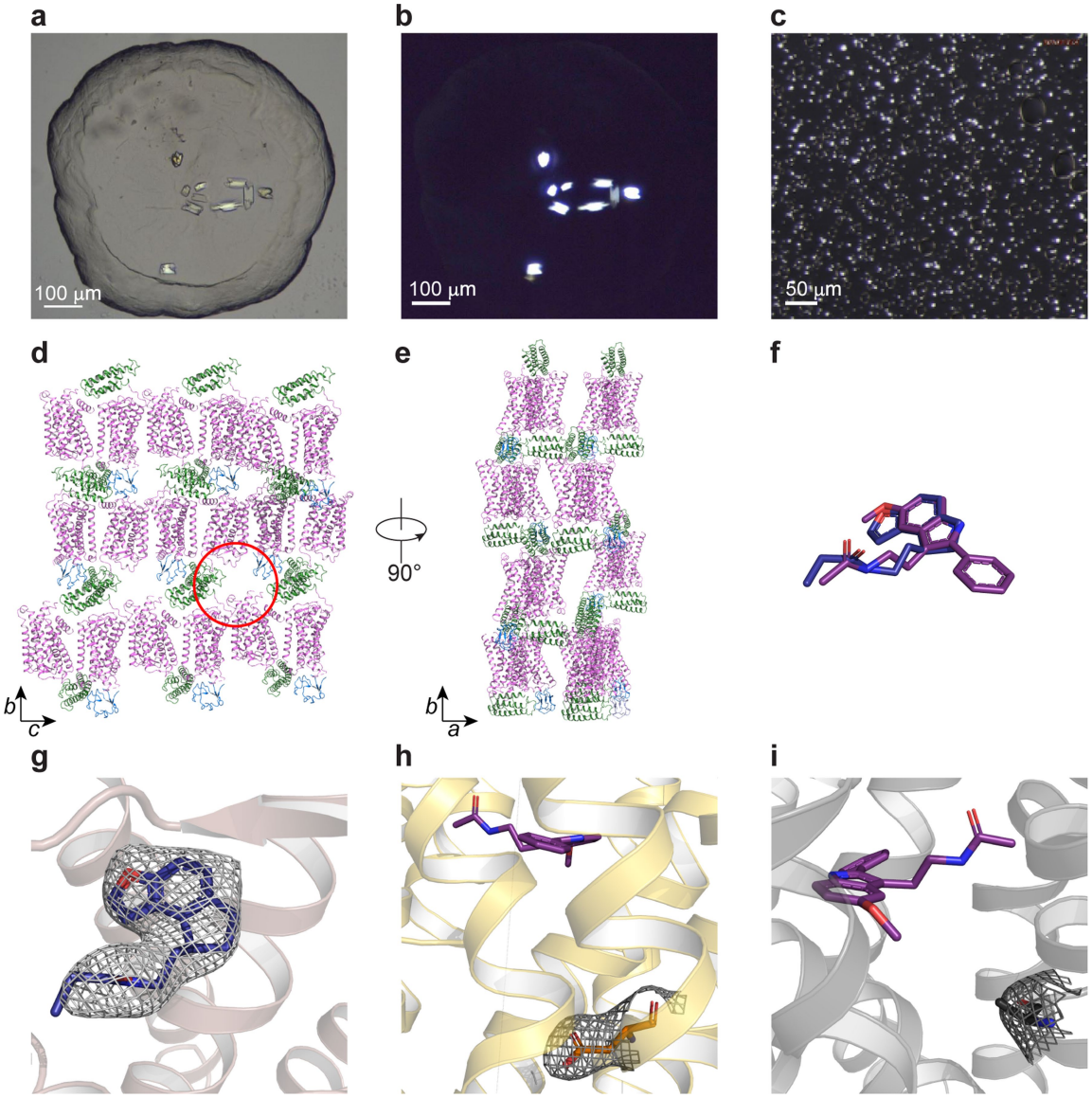

Extended Data Fig. 1 | Crystallization of MT_2: crystals, crystal packing and electron density. a, **b**, Bright field (**a**) and cross-polarized images (**b**) of representative MT_2–2-PMT crystals optimized for synchrotron data collection (representing three independent crystallization setups). **c**, Cross-polarized image of representative MT_2(N86D)–2-PMT crystals used for XFEL data collection (representing three independent crystallization setups). See Extended Data Table 2 for data collection statistics. **d**, **e**, Crystal packing (receptor, purple; BRIL, green; rubredoxin, blue). Space for missing rubredoxin in molecule B of the asymmetric unit is indicated with a red circle. Lattice rotated 90° is shown in **e**. **f**, Overlay of 2-PMT (purple) and ramelteon (blue) ligands of MT_2. **g**–**i**, $2mF_o - DF_c$ density (grey) contoured at 1σ of ramelteon (**g**), N86$^{2.50}$D mutation (**h**), and H208$^{5.46}$A mutation (**i**). 2-PMT is shown in purple.

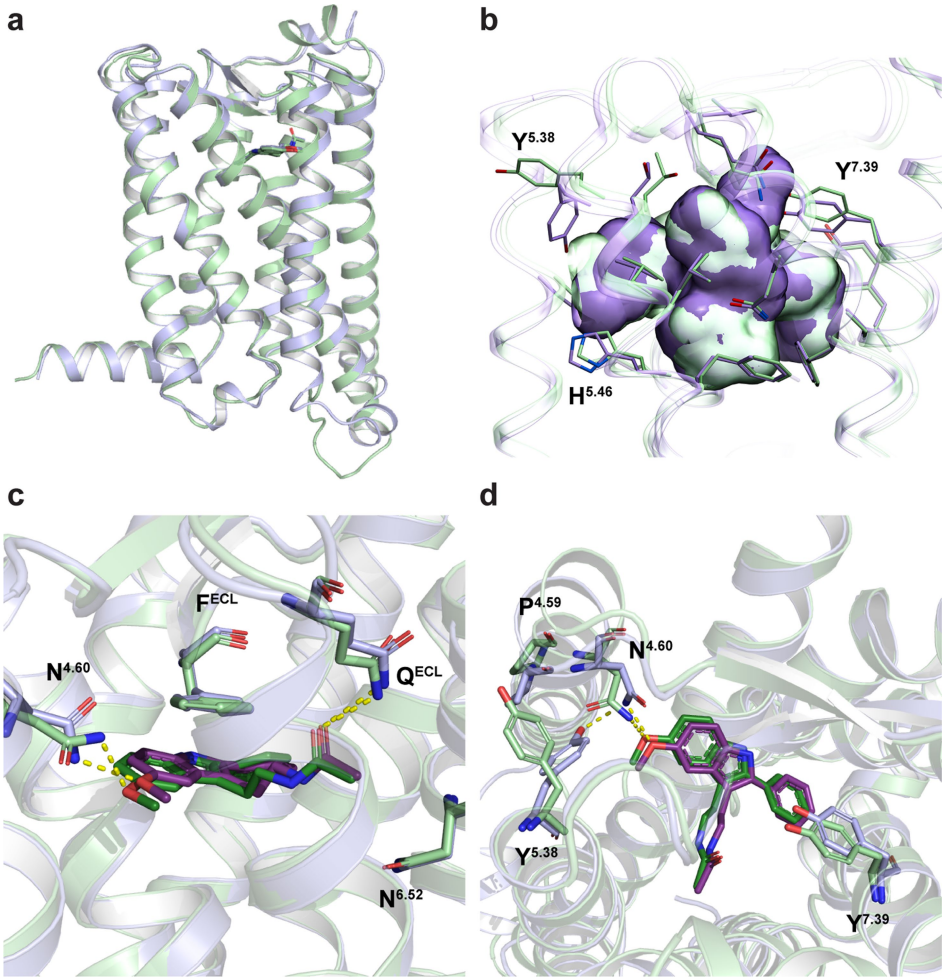

Extended Data Fig. 2 | Structural differences between MT_1 and MT_2. **a**, Overlay of MT_1–2-PMT (green) and MT_2–2-PMT (violet) structures (Cα r.m.s.d = 0.6 Å). **b**, Comparison of MT_1 (green) and MT_2 (violet) binding pockets. Overall, the binding pocket in MT_2 is about 50 $Å^3$ larger than in MT_1. **c**, Comparison of 2-PMT ligand conformations in MT_1 (green) and MT_2 (violet). Hydrogen bonds are shown as yellow dashed lines. **d**, Overlay of MT_1 and MT_2, showing residues with different conformations in the vicinity of the binding pocket. $N^{4.60}$ makes a hydrogen bond with $Y^{5.38}$ in MT_2 but not in MT_1.

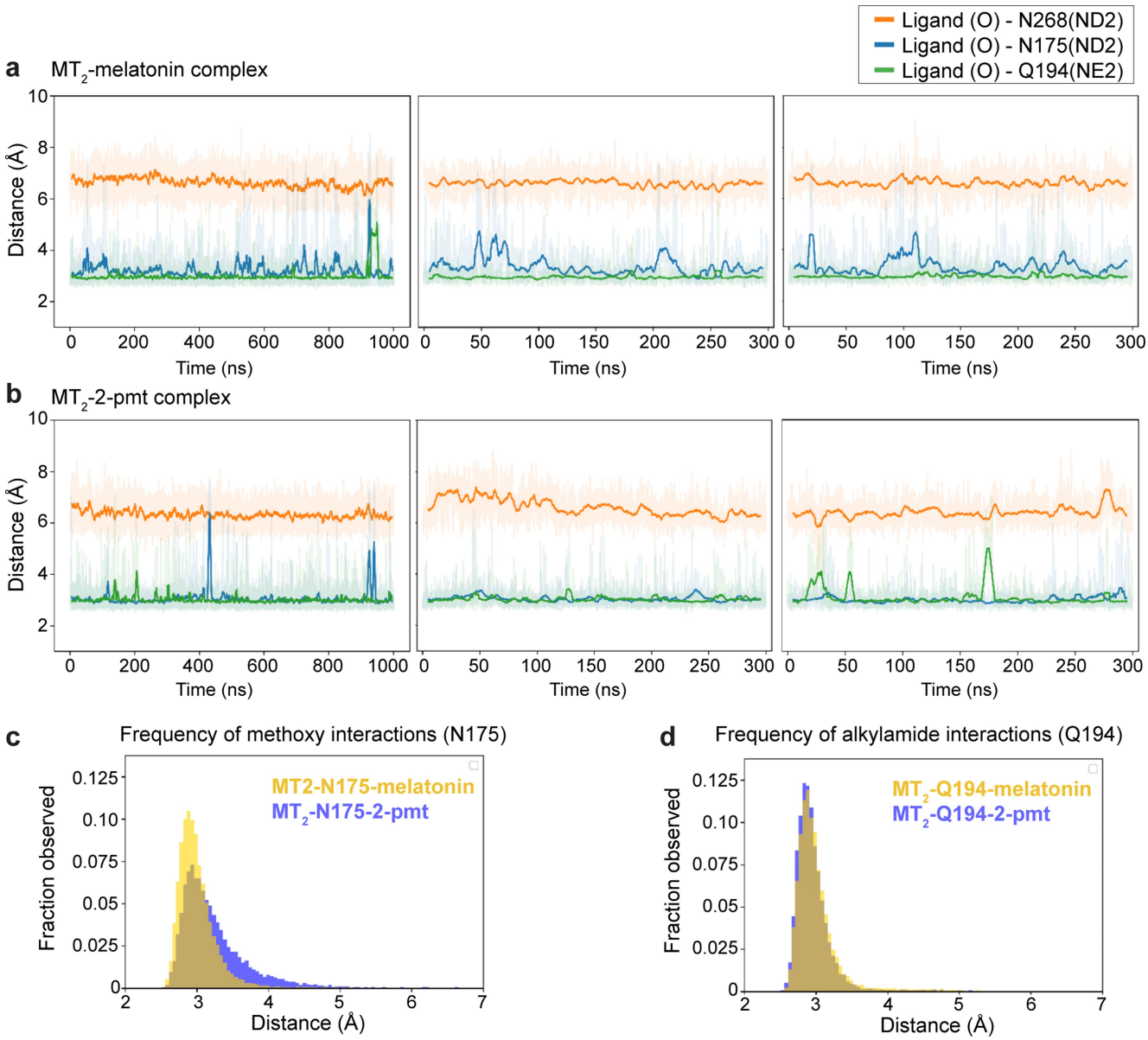

Extended Data Fig. 3 | Molecular dynamics simulations. a, **b**, Distance plots for interactions between residues in MT_2 ($N175^{4.60}$, atom ND2; $Q194^{ECL2}$, atom NE2; $N268^{6.52}$, atom ND2), and closest oxygen atoms of the ligand methoxy and acetyl groups, respectively, in complexes with melatonin (**a**) and 2-PMT (**b**) from three independent simulation runs. **c**, Distance histograms for interactions of $N175^{4.60}$ with methoxy of melatonin (yellow) and 2-PMT (violet). **d**, Distance histograms for interactions of $Q194^{ECL2}$ with alkylamide tail of melatonin (yellow) and 2-PMT (violet).

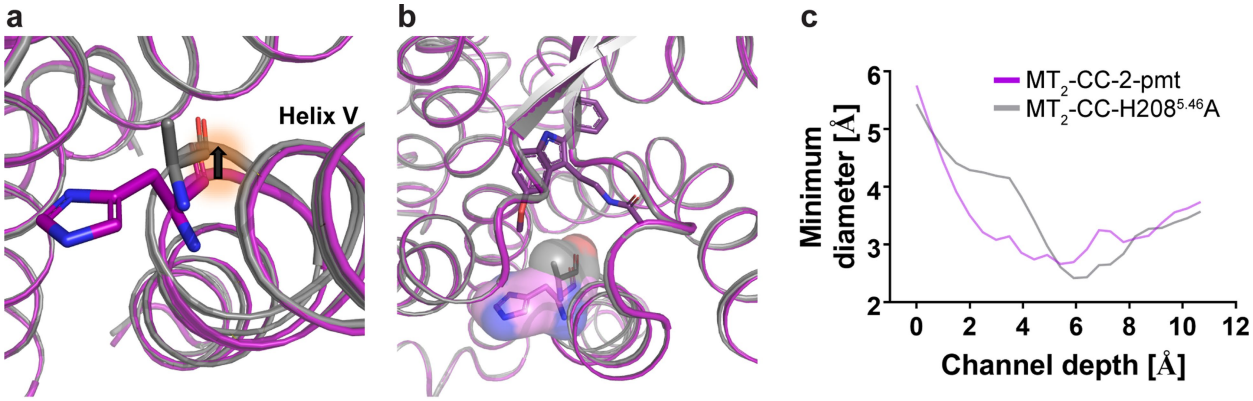

d

Mutant	melatonin			CTL 01-05-B-A05		
	EC_{50}, nM [n] (pEC_{50} ± s.e.m.)	$\%E_{MAX}$ ($\%E_{MAX}$*)	$\Delta\log(E_{MAX}/EC_{50})$ (mutant-wt)	EC_{50}, nM [n] (pEC_{50} ± s.e.m.)	$\%E_{MAX}$ ($\%E_{MAX}$*)	$\Delta\log(E_{MAX}/EC_{50})$ (mutant-wt)
WT	0.028 [16] (10.56±0.09)	100 (100)	0	16.59 [6] (7.78±0.07)	100 (63±7)	0
H208A (5.46)	0.190 [9] (9.72±0.26)	80±9	-0.93	*No agonist activity*		

Extended Data Fig. 4 | Structural and functional differences between MT_2–2-PMT and $MT_2(H208A^{5.46})$–2-PMT. a, Overlay of the MT_2–2-PMT (purple) structure with that of $MT_2(H208^{5.46}A)$–2-PMT (grey) reveals an inward shift of helix V of about 0.9 Å, due to the $H208^{5.46}A$ mutation (black arrow). **b**, Surface representation of the $H208^{5.46}$ and $H208^{5.46}A$ residues. Rotation of helix V renders the binding pocket volume about 50 $Å^3$ smaller for the $H208^{5.46}A$ structure (binding site volume for MT_2–2-PMT: 766 $Å^3$ compared to 716 $Å^3$ for the $MT_2(H208^{5.46}A)$–2-PMT structure). **c**, Comparison of the channel profiles (from the outside of the protein towards the ligand) for MT_2–2-PMT (purple) and $MT_2(H208^{5.46}A)$–2-PMT (grey) reveals a narrowing of the $MT_2(H208^{5.46}A)$–2-PMT channel at a depth of around 6 Å as a consequence of the mutation and subsequent inward rotation of helix V. **d**, Functional data for wild-type and $H208^{5.46}A$ mutant MT_2 expressed in HEK293T cells by using GloSensor to measure $G_{i/o}$-mediated inhibition of cAMP. Data represent mean ± s.e.m. for *n* independent experiments as indicated in square brackets. $\%E_{MAX}$ (maximum effect of a drug) is relative to wild-type receptor (in columns), and $\%E_{MAX}*$ is relative to melatonin activity (in rows). See Methods for further information and Supplementary Fig. 6 for dose–response curves.

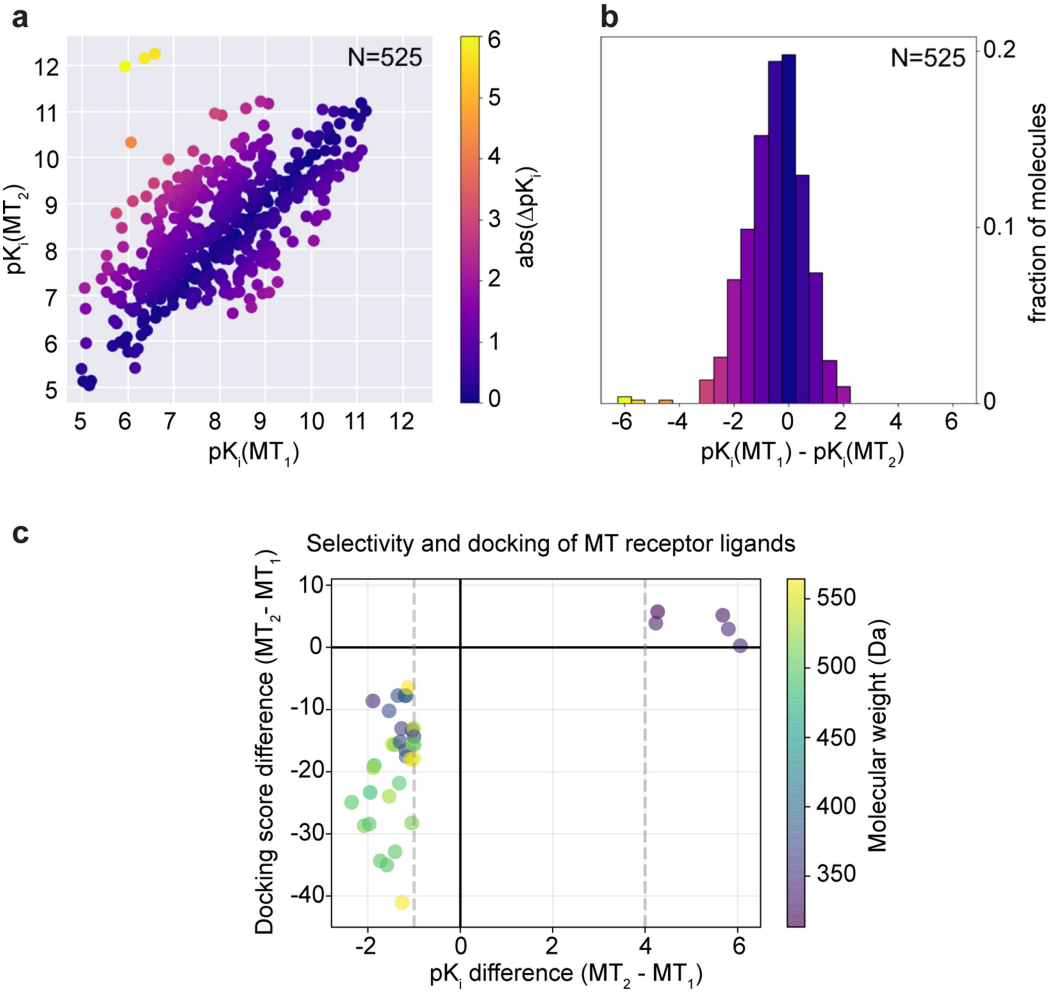

Extended Data Fig. 5 | Selectivity analysis of melatonergic compounds. **a**, Binding affinities of ligands for MT_1 (ChEMBL target identifier CHEMBL1945) and MT_2 (CHEMBL1946) were retrieved from the ChEMBL database[15] (v. 24) of experimental literature values. Of these ligands, 525 have affinities reported for both receptor subtypes. For ligands with multiple reported affinity values for a given receptor, pK_i values were averaged. MT_1-selective ligands are in the lower right quadrant; MT_2-selective ligands are in the upper left quadrant. Data points are coloured by absolute pK_i difference between subtypes (that is, selectivity). **b**, Histogram of observed ligand selectivities. MT_2 selective ligands are on the left of the panel, MT_1 selective ligands are on the right. **c**, Plot of the docking score difference of select ligands that were docked between MT_2 and MT_1 versus their pK_i difference (MT_2 – MT_1). Dashed lines indicate pK_i selectivity cutoff criteria (MT_1: −1 and MT_2: 4). Data points are coloured by molecular mass (Da). See Supplementary Table 1 for details of docked ligands.

Extended Data Table 1 | Ligand affinity data for MT_2 mutants

Mutant	melatonin	2-pmt	ramelteon	agomelatine
	Kd, nM [n] (pK_d ±s.e.m.)	Ki, nM [n] (pK_i ±s.e.m.)	Ki, nM [n] (pK_i ±s.e.m.)	Ki, nM [n] (pK_i ±s.e.m.)
WT	0.54 [10] (9.27±0.12)	0.17 [10] (9.78±0.11)	0.23 [4] (9.66±0.10)	0.24 [4] (9.63±0.08)
WT + NaCl	1.56 [6] (8.81 ± 0.18)	ND	ND	ND
MT_2-CC (Sf9)	63.10 [3] (7.20±0.06)	3.14 [4] (8.50±0.06)	2.60 [4] (8.59±0.02)	6.88 [4] (8.16±0.05)
MT_2-CC (sf9) + NaCl	48.23 [3] (7.32±0.03)	ND	ND	ND
MT_2-CC-N86$^{2.50}$D (Sf9)	29.40 [6] (7.53±0.34)	6.46 [4] (8.19±0.15)	7.37 [4] (8.13±0.09)	26.76 [4] (7.57±0.05)
MT_2-CC-H208$^{5.46}$A (Sf9)	10.81 [6] (7.97±0.16)	3.57 [6] (8.45±0.03)	2.03 [6] (8.69±0.13)	4.98 [6] (8.30±0.04)
D86N (2.50)	5.80 [3] (8.24±0.04)	0.33 [3] (9.48±0.12)	ND	ND
D86N (2.50) + NaCl	3.26 [3] (8.49±0.09)	ND	ND	ND
L108F (ECL1)	0.94 [3] (9.03±0.11)	0.13 [3] (9.87±0.15)	ND	ND
F129W (3.41)	2.84 [3] (8.55±0.04)	0.22 [3] (9.65±0.08)	ND	ND
N137D (3.49)	1.24 [3] (8.91±0.13)	0.12 [3] (9.92±0.00)	ND	ND
C140L (3.52)	0.21 [3] (9.68±0.05)	0.03 [3] (10.50±0.02)	ND	ND
W264F (6.48)	0.88 [3] (9.06±0.14)	0.06 [3] (10.25±0.26)	ND	ND
A305P (7.50)	3.94 [3] (8.40±0.19)	0.47 [3] (9.32±0.06)	ND	ND
N312D (7.57)	2.85 [3] (8.54±0.07)	0.36 [3] (9.44±0.04)	ND	ND
P95A (2.59)	*No specific binding up to 7 nM [^{3}H]-melatonin*			
M120A (3.32)	0.44 [3] (9.42±0.16)	0.028 [3] (10.7±0.3)	0.055 [3] (10.28±0.09)	0.052 [3] (10.35±0.18)
N175A (4.60)	0.86 [3] (9.2±0.3)	0.09 [3] (10.06±0.06)	0.08 [3] (10.12±0.11)	0.25 [3] (9.60±0.04)
F192A (ECL2)	*Low expression, no specific binding up to 7 nM [^{3}H]-melatonin*			
F192I (ECL2)	*No specific binding up to 7 nM [^{3}H]-melatonin*			
Q194A (ECL2)	0.62 [3] (9.4±0.3)	0.043 [3] (10.38±0.07)	0.051 [3] (10.4±0.2)	0.12 [3] (9.94±0.09)
Y200A (5.38)	0.63 [3] (9.3±0.3)	0.14 [3] (9.86±0.01)	0.19 [3] (9.73±0.03)	0.67 [3] (9.18±0.02)
A203F (5.41)	0.82 [5] (9.09±0.01)	0.12 [5] (9.94±0.06)	0.19 [5] (9.47±0.19)	0.42 [5] (9.37±0.19)
H208A (5.46)	1.24 [3] (8.94±0.13)	0.17 [3] (9.79±0.09)	0.18 [3] (9.77±0.11)	0.22 [3] (9.68±0.11)
N268A (6.52)	0.96 [3] (9.3±0.4)	0.09 [3] (10.08±0.09)	0.12 [3] (9.92±0.05)	0.20 [3] (9.69±0.03)
Y294A (7.39)	1.07 [3] (8.99±0.09)	0.042 [3] (10.38±0.04)	0.049 [3] (10.33±0.09)	0.10 [3] (10.04±0.10)
Y308S (7.53)	*No specific binding up to 7 nM [^{3}H]-melatonin*			

Data were acquired with wild-type (WT) MT_2 and mutants expressed in HEK293T cells by radioligand competition binding using [^{3}H]melatonin to yield K_d or K_i affinity estimates. Data represent mean ± s.e.m. for *n* independent experiments as indicated in square brackets. Crystal constructs (CC) were expressed in Sf9 cells. ND, not determined. Binding isotherms are shown in Supplementary Fig. 2. For determining the effect of NaCl, binding assays were performed in the presence of 147 nM NaCl (binding isotherms in Supplementary Fig. 3).

Extended Data Table 2 | MT_2 Crystallographic data collection and refinement statistics

	MT_2-CC-2-pmt[a]		MT_2-CC-H208$^{5.46}$A-2-pmt[b]		MT_2-CC-N86$^{2.50}$D-2-pmt[c]		MT_2-CC-ramelteon[d]	
Data collection								
Space group	$P2_1$		$P2_1$		$P2_1$		$P2_1$	
Cell dimensions								
a, b, c (Å)	69.5, 146.2, 77.3		69.2, 146.2, 77.3		68.7, 145.8, 77.0		69.4, 145.7, 77.2	
α, β, γ (°)	90, 111.7, 90		90, 105.2, 90		90, 107.4, 90		90, 106.2, 90	
Resolution (Å)	21.99-2.80 (2.88-2.80)		21.99-3.20 (3.34-3.20)		22.0-3.10 (3.23-3.10)		22.0-3.30 (3.46-3.30)	
R_{split}	0.146 (4.31)		0.181 (3.26)		0.189 (4.70)		0.201 (2.90)	
$I/\sigma I$	3.07 (0.46)		4.02 (0.39)		3.87 (0.3)		3.67 (0.42)	
CC*	0.999 (0.52)		0.997 (0.54)		0.997 (0.60)		0.997 (0.54)	
Completeness (%)	100 (100)		100 (100)		100 (100)		100 (100)	
Redundancy	571.2 (141.3)		196.6 (39)		133 (38.2)		221.1 (84.6)	
Refinement								
Resolution (Å)	21.99-2.80		21.99-3.20		22.0-3.10		22.0-3.30	
No. reflections	35,193		24,439		26,179		22,122	
R_{work}/R_{free}	0.219/0.249		0.224/0.250		0.234/0.262		0.248/0.270	
No. atoms	A	B	A	B	A	B	A	B
Protein	3,333	2,852	3,343	2,786	3,293	2,752	3,227	2,738
Ligand/Zn^{+2}	23/1	23/0	23/1	23/0	23/1	23/0	19/1	19/0
Lipid and other	0	11	0	12	0	0	0	0
B-factors (Å^2)								
Receptor	116.4	121.0	95.0	99.6	114.2	117.2	114.1	118.2
BRIL	162.3	188.9	143.2	176.4	167.6	208.8	185.3	248.1
Rubredoxin	114.7	n/a	100.3	n/a	116.2	n/a	118.6	n/a
Ligand/Zn^{+2}	101.6/114.7	106.1/n/a	73.3/91.2	88.7/n/a	96.9/112.3	102.1/n/a	94.9/117.7	105.6/n/a
Lipids and other	n/a	138.8	n/a	111.0	n/a	n/a	n/a	n/a
R.m.s. deviations								
Bond lengths (Å)	0.009		0.010		0.009		0.009	
Bond angles (°)	0.97		1.06		0.96		0.95	

Number of crystals used for structure determination: [a]31,677, [b]28,130, [c]20,704 and [d]28,834. Values in parentheses are for highest-resolution shell.

Extended Data Table 3 | Functional data ($G_{i/o}$ GloSensor) for MT_2 crystal construct mutants

Mutant	melatonin			2-pmt		
	EC_{50}, nM [n] (pEC_{50} ±s.e.m.)	$\%E_{MAX}$ ($\%E_{MAX}$*)	$\Delta\log(E_{MAX} / EC_{50})$ (mutant-WT)	EC_{50}, nM [n] (pEC_{50} ±s.e.m.)	% E_{MAX} ($\%E_{MAX}$*)	$\Delta\log(E_{MAX} / EC_{50})$ (mutant-WT)
WT	0.028 [16] (10.56±0.09)	100 (100)	0	0.018 [14] (10.75±0.11)	100 (100±5)	0
MT_2-CC (Sf9)	*No activity*					
MT_2-Rub	*No activity*					
D86N (2.50)	3.951 [3] (8.40±0.34)	80±18 (100)	-2.25	1.995 [3] (8.70±0.11)	101±17 (126±21)	-2.04
L108F (ECL1)	0.029 [5] (10.54±0.10)	72±4 (100)	-0.16	0.011 [6] (10.95±0.19)	80±8 (110±11)	0.11
F129W (3.41)	0.011 [6] (10.95±0.17)	128±9 (100)	+0.50	0.007 [6] (11.16±0.20)	128±7 (99±6)	0.52
N137D (3.49)	0.019 [6] (10.72±0.12)	88±6 (100)	-0.11	0.016 [6] (10.81±0.10)	90±5 (103±5)	0.19
C140L (3.52)	0.072 [7] (10.15±0.16)	90±8 (100)	-0.46	0.035 [6] (10.45±0.16)	89±6 101±4)	-0.34
W264F (6.48)	0.044 [7] (10.36±0.09)	117±6 (100)	-0.13	0.020 [5] (10.70±0.40)	118±8 (101±6)	-0.03
A305P (7.50)	0.141 [7] (9.85±0.16)	129±5 (100)	-0.60	0.073 [5] (10.14±0.26)	143±4 (91±6)	-0.45
N312D (7.57)	0.069 [5] (10.16±0.15)	135±6 (100)	-0.26	0.041 [3] (10.39±0.18)	138±10 (102±8)	-0.21

Data were acquired with wild-type MT_2 and mutants expressed in HEK293T cells by using GloSensor to measure $G_{i/o}$-mediated cAMP inhibition via isoproterenol stimulation. Data represent mean ± s.e.m. for *n* independent experiments as indicated in square brackets. $\%E_{MAX}$ is relative to wild-type receptor (in columns), and $\%E_{MAX*}$ is relative to melatonin (in rows). Mutant effects were calculated by the change in relative activity or $\log(Emax/EC_{50})$, subtracting wild type from mutant. Dose–response curves are shown in Supplementary Fig. 4.

Extended Data Table 4 | Functional data ($G_{i/o}$ GloSensor) for MT_2 mutants

	melatonin			2-pmt			ramelteon			agomelatine		
Mutant	EC_{50}, nM [n] (pEC_{50} ±s.e.m.)	% E_{MAX} (%E_{MAX}*)	Δlog(E_{MAX} / EC_{50}) (mutant-wt)	EC_{50}, nM [n] (pEC_{50} ±s.e.m.)	% E_{MAX} (%E_{MAX}*)	Δlog(E_{MAX} / EC_{50}) (mutant-wt)	EC_{50}, nM [n] (pEC_{50} ±s.e.m.)	% E_{MAX} (%E_{MAX}*)	Δlog(E_{MAX} / EC_{50}) (mutant-wt)	EC_{50}, nM [n] (pEC_{50} ±s.e.m.)	% E_{MAX} (%E_{MAX}*)	Δlog(E_{MAX} / EC_{50}) (mutant-wt)
WT	0.028 [16] (10.56±0.09)	100 (100)	0	0.018 [12] (10.75±0.11)	100 (100±4)	0	0.016 [12] (10.81±0.14)	100 (108±3)	0	0.018 [10] (10.75±0.12)	100 (105±4)	0
P95A (2.59)	*No activity*											
A171M (4.56)	0.075 [9] 10.13±0.14	66±9 (100)	-0.61	0.032 [8] 10.49±0.11	62±9 (94±14)	-0.46	0.031 [7] 10.51±0.19	67±9 (90±12)	-0.47	0.025 [6] 10.60±0.16	75±10 (107±15)	-0.27
N175A (4.60)	0.070 [9] (10.16±0.15)	74±10 (100)	-0.53	0.0192 [8] (10.72±0.12)	67±14 91±19	-0.20	0.010 [7] (11.00±0.21)	72±12 (87±14)	+0.05	0.015 (7] (10.82±0.13)	71±7 (91±10)	0.08
F192A (ECL2)	99.235 [6] (7.00±0.26)	122±7 (100)	-3.46	4.808 [10] 8.32±0.09	139±3 (114±6)	-2.28	4.799 [9] 8.32±0.04	150±4 (109±3)	-2.31	5.316 [9] 8.27±0.05	145±2 (111±2)	-2.31
F192I (ECL2)	3.00 [3] (8.52±0.30)	159±4 (100)	-1.83	0.211 [3] (9.68±0.07)	159±3 (100±1)	-0.87	0.571 [3] (9.24±0.16)	169±5 (94±3)	-1.34	2.754 [3] (8.56±0.05)	160±8 (94±5)	-1.98
Q194A (ECL2)	0.025 [3] (10.60±0.22)	131±4 (100)	+0.16	0.011 [3] (10.96±0.08)	130±3 (99±3)	+0.33	0.006 [3] (11.23±0.10)	130±6 (88±4)	+0.54	0.005 [3] (11.30±0.13)	110±15 (78±10)	+0.59
Y200A (5.38)	0.517 [3] (9.29±0.32)	161±10 (100)	-1.06	0.009 [3] (11.07±0.08)	158±16 (98±10)	+0.53	0.014 [3] (10.86±0.07)	164±21 (90±10)	0.26	0.314 [3] (9.50±0.31)	149±14 (87±8)	-1.07
H208A (5.46)	0.190 [9] (9.72±0.26)	80±9 (100)	-0.93	0.101 [10] (10.00±0.15)	75±9 (93±11)	-0.88	0.035 [8] (10.45±0.28)	79±11 (88±12)	-0.46	0.083 [8] (10.08±0.26)	76±2 (89±3)	-0.79
N268A (6.52)	0.046 [3] (10.33±0.27)	141±10 (100)	-0.08	0.013 [3] (10.87±0.10)	140±8 (99±6)	+0.28	0.009 [3] (11.05±0.10)	132±9 (83±6)	+0.36	0.007 [3] (11.16±0.10)	112±4 (75±3)	+0.46
Q194A (ECL2)/ N268A (6.52)	2.405 [9] 8.62±0.21	116±7 (100)	-1.88	0.033 [10] 10.49±0.18	112±6 (96±5)	-0.21	0.136 [9] 9.87±0.15	121±7 (93±5)	-0.86	0.759 [8] 9.12±0.14	116±4 (94±4)	-1.56
Y294A (7.39)	0.460 [4] (9.34±0.15)	148±6 (100)	-1.05	0.008 [4] (11.12±0.11)	153±7 (94±9)	+0.56	0.008 [3] (11.11±0.09)	153±11 (114±11)	+0.48	0.015 [3] (10.83±0.20)	118±11 (143±12)	-0.15
Y308S (7.53)	*No activity*											

Data were acquired with MT_2 mutants by using GloSensor to measure $G_{i/o}$-mediated cAMP inhibition via isoproterenol stimulation. Data represent mean ± s.e.m. for *n* independent experiments as indicated in square brackets. %E_{MAX} is relative to wild-type receptor (in columns), and %E_{MAX*} is relative to melatonin (in rows). Mutant effects were calculated by the change in relative activity, or log(E_{MAX}/EC_{50}) subtracting wild-type from mutant. ND, not determined. Dose–response curves are shown in Supplementary Fig. 5.

Extended Data Table 5 | Thermostability data for MT_2 mutants

Mutant	apo Tm, °C	mlt Tm, °C	2-pmt Tm, °C	mlt ΔTm, °C	2-pmt ΔTm, °C
MT_2-CC	63.6±0.3	73.4±0.1	79.9±0.4	+9.8	+16.3
W129F (3.41)	59.0±0.2	72.4±0.1	78.9±0.3	+13.4	+19.9
N175A (4.60)	64.6±0.3	70.6±0.1	78.1±0.2	+6	+13.5
F192A (ECL2)	57.1±0.5	66.5±0.1	75.4±0.1	+9.4	+18.3
Q194A (ECL2)	65.5±0.3	69.9±0.3	77.3±0.2	+4.4	+11.8
H208A (5.46)	58.7±0.6	72.6±0.4	78.9±0.3	+13.9	+20.2
N268A (6.52)	63.3±0.3	66.1±0.2	74.6±0.3	+2.8	+11.3
Q194A (ECL2)/N268A (6.52)	67.9±0.3	67.9±0.1	71.4±0.3	0	+3.5
Y308S (7.53)	ND	65.5±0.2	75.8±0.3	ND	ND

Melting temperature T_m determined using the CPM assay[28] (mean ± s.d. for $n = 3$ independent experiments) for the crystallized construct (MT_2-CC), and indicated mutants (in the MT_2-CC background), purified in the absence (apo) or presence (100 μM) of ligand (mlt, melatonin and 2-PMT, 2-phenylmelatonin). ND, not determined. W129F refers to MT_2-CC but without the $F129^{3.41}W$ mutation. Melting curves are shown in Supplementary Fig. 7.